Smart Materials and Structures

Crossmark

RECEIVED 18 September

dd Month yyyy

DADED

Proof of Concept of a Tunable Suspension Using a Temperature-Driven Polymer

J. Roberjot^{1,3}, E. Sadoulet-Reboul¹, N. Peyret², E. Bachy³, C. Arnould³, E. Collard³, K. Jaboviste ¹ and G. Chevallier⁴

E-mail: Corresponding author: johann.roberjot@gmail.com

E-mail: emeline.sadoulet-reboul@univ-fcomte.fr

Keywords: suspension, temperature-driven material, thermal control

Abstract

Vibration isolation consists in attenuating the transfer of vibrations between two systems by means of a suspension system. The analysis of the different life cycles shows that for suspension to function optimally, the cutoff frequency should vary according to operating conditions, and comfort, performance or integrity objectives. Thus a well-tuned suspension system should be capable of adapting its stiffness to meet varying isolation requirements. This paper proposes a proof-of-concept for a suspension integrating a temperature-driven polymer which is used to adjust the cutoff frequency. A numerical finite element model is developed to design the system and to assess its performance under various thermal and mechanical contact conditions. The results demonstrate that a large tunability of the resonant frequency of the structure can be obtained changing the applied temperature. They are validated through a dedicated experimental campaign. Overall, this work paves the way for a novel adaptive suspension concept based on a smart polymer with temperature-driven properties.

1 Introduction

Suspension systems aim at preventing the vibration transfer from a host structure to embedded devices in order to stabilize equipment. This characteristic is crucial for a whole range of applications, in many industrial fields: aeronautics, space, defense, automotive, rail and medical, where precision and stability are paramount. Indeed, high-precision optical instruments are commonly embedded within structures and the challenge is to maintain their functionality, accuracy, and integrity despite the static loadings (weight) and the dynamic loadings (vibrations and shocks). In this context, suspensions are designed to filter out vibrations while maintaining the rigidity required to support weight and shocks. A trade-off has thus to be found between stiffness and flexibility. Generally speaking, suspensions are only designed to achieve a low cutoff frequency, in order to guarantee their filtering efficiency over a wide frequency band. This configuration results in low static rigidity. As a result, displacements under static and low-frequency loads are high. This calls into question mechanical resistance under loads such as shock.

The aim, therefore, is to define a suspension with high stiffness under quasi-static loading conditions, while allowing greater flexibility and compliance in response to dynamic forces. Such an adaptive suspension is likely to adapt to varying environmental conditions, providing a balance between stiffness and flexibility as required. By combining the advantages of high static stiffness and low dynamic stiffness, these systems maintain optimum performance over a wide range of operating conditions.

A strategy widely developed in the literature to get the required adaptive behavior is the Quasi-Zero Stiffness (QZS) suspension. Such structures are based on a arrangement of components with positive and negative stiffnesses designed to exhibit near-zero stiffness characteristics under certain conditions, particularly when subjected to low-frequency or static loads. It is particularly efficient to

¹Université Marie et Louis Pasteur, CNRS, institut FEMTO-ST, F-25000 Besançon, France

 $^{^2 \}mathrm{ISAE}\text{-Supm\'e}\mathrm{ca},$ Laboratoire QUARTZ EA 7393 - F-93400 Saint-Ouen, France

³THALES LAS France, F-78990, Elancourt, France

⁴Centre de recherche de l'École de l'air et de l'espace, École de l'air et de l'espace, F-13660 Salon-de-Provence, France

59 60

effectively isolate the associated payload from mechanical shocks. At the same time, the suspension maintains a level of flexibility under vibrations to accommodate to dynamic loads. Different technologies are investigated in the literature to integrate nonlinearities and create the negative stiffness effect as the use of multiple springs into different directions [Alabuzhev, 1989, Carrella et al., 2007], the buckling of elastic elements as beams or composite laminates [Liu et al., 2013], the use of magnets [Dong et al., 2017, Wang et al., 2023], bistable plates [Li et al., 2022], cam-rollers [Li et al., 2021, Zuo et al., 2022], origami structures [Ye et al., 2023, Han et al., 2023], or again lever-type mechanism [Kocak and Yilmaz, 2023]. The research advances around technologies and applications for QZS suspensions are detailed in Liu et al. [2024]. Recent studies, inspired by biology and the behavior of limbs and legs of animals, include X-shaped structures with tunable properties [Chai et al., 2022]. QZS resonators have also been introduced into metamaterial plates to control wave propagation at low frequencies [Cai et al., 2022a,b, Xu and Jing, 2024], and generate very low frequency bandgaps. The development of additive manufacturing now offers the opportunity to conceive more complex customized suspensions [Xiao et al., 2024], introducing for instance specific continuous structures with integrated components. One difficulty is that the modeling of such devices can be hard due to uncertainties in the material behavior or damping conditions, which complicates any preliminary design.

Unlike near-zero stiffness (QZS) suspensions, which rely on geometric non-linearities to achieve high static behavior with low dynamics, we propose to achieve this functionality through a temperaturedependent material. In addition, our system offers a wide variation in stiffness. Unlike QZS systems, which rely on non-linear mechanical responses, our suspension remains structurally linear throughout its operating range. Shape memory alloys (SMA) or shape memory polymers (SMP) are temperaturedependent material. Indeed, thanks to their properties at the microscale, they have the ability to change their stiffness, damping, or shape, in response to changes in temperature. They have been used to develop morphing functionnalities [Sun et al., 2021, Kalat et al., 2023], or for vibration control [Butaud et al., 2016, Candido de Sousa et al., 2018, Jaboviste et al., 2019, Chuang et al., 2019, Zhao et al., 2022].

In this context, the aim of this research is a new type of suspension whose stiffness can be adjusted using a temperature-controlled polymer. A proof-of-concept is developed for the case of a complex 3D structure. In the proposed system, basic stiffness is provided by metallic dampers with constant stiffness, while tunability is ensured by an additional damper incorporating a thermally-controllable polymer. The paper is organized as follows. Section 1 presents the state of the art. Section 2 presents the polymer chosen for the study and details its behavior as a function of temperature. Section 3 presents the suspension design scheme and the numerical studies carried out to identify the appropriate material parameters. Finally, Section 4 presents the experimental validation used to evaluate the suspension's performance. For ease of reading, we have included a number of items in the appendices.

$\mathbf{2}$ Description of the temperature-driven polymer

The choice of stiffness adjustment mechanism depends on several criteria: range of stiffness variation, time constant, ease of technological implementation, see table 1. In our case, the stiffness variation was the dominant factor. This section presents the tBA-PEGDMA polymer used in this study, which offers structural adjustability.

Presentation of the polymer

Any viscoelastic material exhibiting temperature dependency is a potential candidate for the design of an adaptive damper. The polymer tBA-PEGDMA is selected in this paper due to its remarkable properties as documented by Srivastava et al. [2010] and characterized in several articles by Butaud et al. [2018] and Jaboviste et al. [2019]. It exhibits a significant stiffness variation (x3000) between the glassy and rubbery states, providing a more adaptable response to temperature changes compared to Shape Memory Alloys (x4). Moreover tBA-PEGDMA allows for a pretty fast change of stiffness, making it interesting for our application. Manufacturing and chemical aspects about tBA-PEGDMA are presented in appendix A

Technology	Stiffness controllability	Tuning mech- anism	Time constant	Implementation
SMP (Shape Memory Polymer)	Young modulus 0.7 - 2000 MPa (x 3000)	Heating / cooling system	tc = 1-100s (depends on heating power)	Simple molding, lightweight; heating/cooling system; limited cycling stability
Air spring	Pressure 0.1 - 1.0 MPa (x 10)	Pressure and volume change	tc = 0.1-1s (depends on compressor power)	Mature technology; compressor, valves; large-scale suspensions
SMA (Shape Memory Alloy)	Young modulus 30 - 90 GPa (x3)	Thermally induced phase transformation	tc = 0.1-10 s (depends on heating power)	High energy density; requires thermal control; hysteresis; lim- ited fatigue life

Table 1: Comparison of baseline stiffness, tuning mechanism, response speed, and implementation aspects for SMPs, air springs, and SMAs.

2.2 Rheological model

The mechanical behavior is represented using a viscoelastic 2S2P1D model, which is characterized by two Springs (2S), two Parabolic creep elements (2P) and one Dashpot (1D), see Butaud et al. [2018]. The global complex modulus E^* is written as,

$$E^* = E_0 + \frac{E_\infty - E_0}{1 + \gamma (j\omega\tau)^{-k} + (j\omega\tau)^{-h} + (j\omega\beta\tau)^{-1}}.$$
 (1)

 E_0 represents the rubber modulus as ω approaches 0, while E_∞ denotes the glassy modulus as ω tends toward ∞ , k and h are exponents with 0 < k < h < 1 represented as two parabolic creep elements, γ and β are dimensionless constants. τ is the characteristic time, which is estimated with the time-temperature superposition principle,

$$\tau(T) = a_T(T)\tau_0. \tag{2}$$

 $\tau_0 = \tau(T_0)$ is set at a reference temperature T_0 of 313.15 K, and $a_T(T)$ is the shift factor at the temperature T, formulated thanks to the Williams-Landel-Ferry (WLF) law,

$$\log(a_T(T)) = \frac{-C_1^0(T - T_0)}{-C_2^0 + (T - T_0)},\tag{3}$$

with $C_1^0 = 10.87$ and $C_2^0 = 32.57$ K. The validity of the WLF law in this context was also specifically addressed in Butaud et al. [2018], where the identification was carried out across a broad frequency and temperature range, confirming the applicability of the time-temperature superposition principle for this material. Parameters are identified from DMA (Dynamic Mechanical Analysis) tests as decribed in Butaud et al. [2016]. Table 2 contains the parameter's values for the considered tBA/PEGDMA polymer.

Table 2: 2S2P1D model parameters for the tBA/PEGDMA polymer

$E_0(\mathrm{MPa})$	$E_{\infty}(\mathrm{MPa})$	k	h	γ	β	$ au_0(\mathrm{s})$
0.67	2210	0.16	0.79	1.68	3.8e4	0.61

2.3 Evolution of the stiffness with the temperature

The use of the time-temperature superposition principle allows to estimate the evolution of the storage modulus with temperature from the knowledge of the evolution with frequency. Let consider Equation (4) and let define the storage modulus as,

$$E' = \Re(E^*). \tag{4}$$

Figure 1 presents the evolution of the storage modulus on the frequency range of interest, from 1 to 1000 Hz. The stiff configuration is defined for a storage modulus higher than 1 GPa, and the soft one for a modulus below 10 MPa. This classification is based on the typical viscoelastic behavior of polymers across the glass transition. Considering this material, a storage modulus above 1 GPa corresponds to the glassy state, in which the material exhibits a rigid behavior. Conversely, a modulus below 10 MPa is representative of the rubbery state, where the polymer becomes highly flexible and deformable. Thus, the upper limit of temperature to maintain the stiff configuration is set at 30 °C, while the lower limit for the soft configuration is 80 °C.

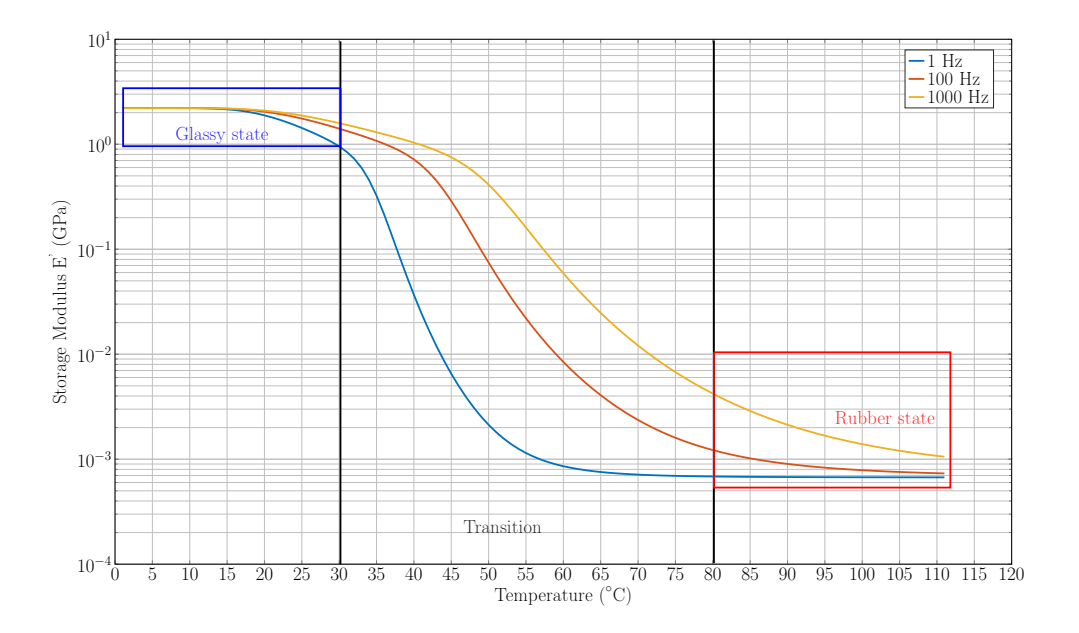


Figure 1: Evolution of the tBA-PEGDMA storage modulus at 1, 100, 1000 Hz and temperature limits to define the configuration. The selected thresholds of 30 °C and 80 °C correspond to storage modulus values consistently above 1 GPa (glassy) and below 10 MPa (rubbery) across the entire working frequency range, ensuring safe design margins independent of excitation rate.

Design of an adaptive suspension integrating a temperature-driven polymer

Architecture of the suspension

The principle of the considered study-case is a payload connected to a base vibrating structure through a suspension composed of three dampers. The central one consists in a thermally-driven damper thanks to the use of the tBA-PEGDMA, while the two others are dampers symmetrically introduced for reference. The CAD Model for the full 3D structure is presented in Figure 2.

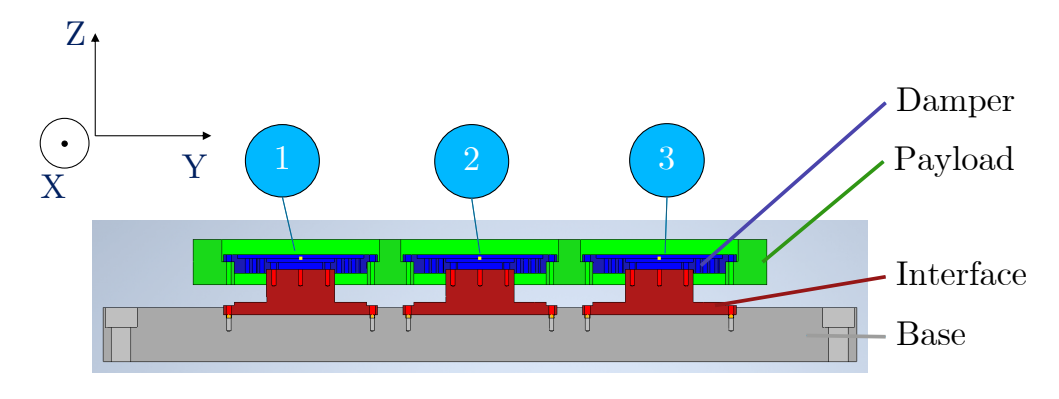


Figure 2: Cross-sectional view of the suspension. Dampers 1 and 3 are made of metal. The damper 2 is loaded with polymer (not shown in this figure) but a zoom of the damper is depicted in Figure).

As the suspension is adapted to a structure representative of the dynamic behaviour of a real optical arm, the exact dimensions and frequencies are not disclosed for confidentiality reasons. Each damper comprises two rings, the smaller inner one is connected to the primary base structure while the outer larger one is linked to the suspended payload. These rings are interconnected by four spiral blades. The design is based on a patented solution by Thales LAS France, [Collard and Fabrice, 2013], comprising a spiral form crafted from 440C steel engineered to possess specific cutoff frequency f_{c0} and eigenfrequency f_{0} under a given mass M. Additionally, this design has been meticulously crafted to fit within a designated area and engineered according to von Mises criteria to withstand specific loads. The Shape Memory Polymer is introduced in the second damper of the suspension as presented in Figure 3: it consists in a thin cylinder machined to fit the inside diameter of the outer ring of the suspension, with holes for attachment to the inner ring of the suspension. The payload, has been designed with two key objectives: firstly, to ensure that the frequencies of its structural modes are far from those of the suspension; and secondly, to align its center of mass with the stiffness center of the blades of the central suspension to minimize the occurrence of tilting modes. The material used for the mobile mass is aluminium.

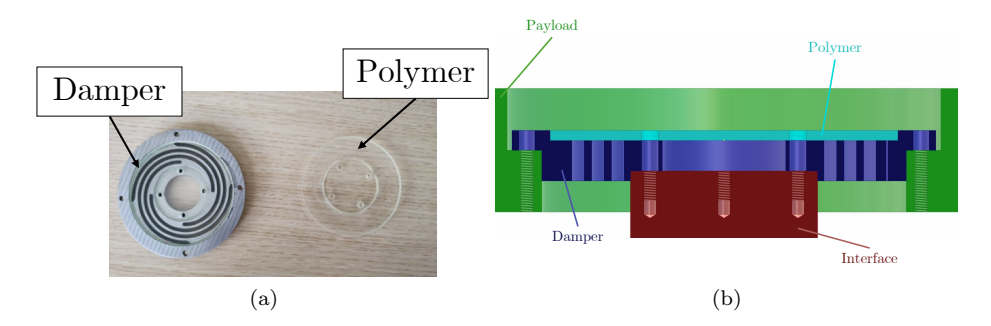


Figure 3: Detailed view for the damper with simplified integration of the temperature-driven polymer (tBA-PEGDMA): (a) Pictures of the damper and polymer part, (b) Enlarged cross-sectional view of the CAD model of the damper connected to the payload (see Figure 2). The interface is connected to a base.

A numerical finite element model of the suspension has been developed to refine the design and evaluate the performance of the proposed proof-of-concept. Material parameters are given in table 3: E is the Young modulus, ν is the Poisson's ratio, ρ is the density, η denotes the loss factor, κ the thermal conductivity, C_p the heat capacity at constant pressure.

Material	E (GPa)	ν	$\rho \; (kg/m^3)$	η	$\kappa (W/(m K))$	$C_p (J/(kg K))$
Aluminium	70	0.33	2700	0.001	238	900
Steel 440C	200	0.33	7750	0.001	44.5	475
polymer	E(f,T)	0.37	990	$\eta(f,T)$	0.12	990

Table 3: Material parameters for the suspension

3.2 Static behavior

To assess the stiffness of the suspension, a stationary numerical simulation has been done. It involves evaluating the equivalent radial stiffness of the damper alone, loaded with polymer, under various temperature stimuli. To accomplish this, the inner ring is fixed, and a force is applied to the outer ring in the longest dimension of the structure, which corresponds to the Y-direction No mass is added and no pre-charge is applied to the rings. The displacement resulting from this force is then evaluated to plot the equivalent radial stiffness of the damper as a function of temperature, as shown in Figure 4. The results show a significant variation in the damper stiffness depending on temperature. The stiffness k = 1.9e5 N/m of the damper at high temperature (120 °C) represents the stiffness required to effectively suspend the payload. The stiffness observed at low temperature (10 °C) k = 6.5e7 N/m corresponds to the stiffness desired for the rigid configuration. This stiffness is found to be 342 times greater than the one at high temperature.

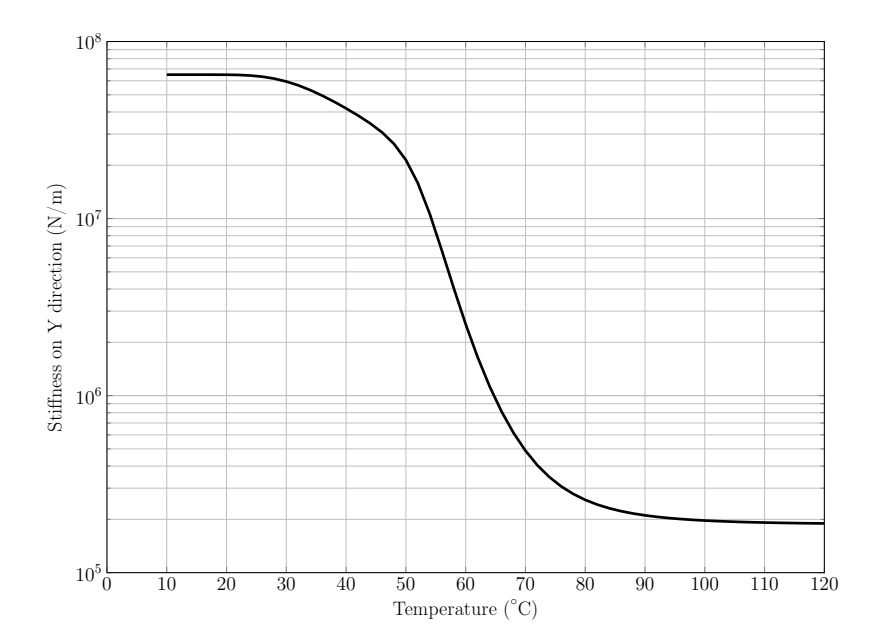


Figure 4: Evolution of the damper stiffness in the Y-direction as a function of temperature.

3.3 Transmissibility behavior

The transmissibility behavior of the suspension is then predicted in the frequency domain. The finite element model (FEM) is established using the CAD presented in figure 3. Considering the viscoelastic elements dependency of temperature and frequency, described by the 2S2P1D model (Section 2.2), a complex stiffness matrix $K^*(T,\omega)$ is introduced, with a temperature (T) and a frequency dependency. So the dynamic discrete equations in the frequency domain can be written as,

$$-\omega^2[M]\hat{X}(\omega) + [K^*(T,\omega)]\hat{U}(\omega) = \hat{F},\tag{5}$$

where M is the mass matrix which is real and constant, \hat{U} the complex displacement vector and \hat{F} is the complex force excitation vector. The complex stiffness matrix K^* is formulated by incorporating the material properties of each element and the connections between them. In the case of the elastic components, such as aluminum and steel, these properties remain constant regardless of frequency or temperature. However, for the viscoelastic components, the material properties of each element, including the storage modulus and the loss factor, vary with temperature and frequency.

The response of the structure is obtained through a direct frequency domain study over a frequency band $[f_a;f_b]$. This response is calculated at several temperatures T, ranging from 20 °C to 85 °C, all 1 °C. In the study, the external force vector \hat{F} is an inertia force due to a sine-sweep excitation at base on the inner ring, with an acceleration amplitude 1 g, where $g=9.81\,\mathrm{m/s^2}$. As for the static study, the excitation direction is the Y-direction (Figure 2). This excitation specifically activates the pure translation mode along the Y-direction. Its purpose is to facilitate the observation of the radial contribution of the three dampers and to evaluate the impact of temperature on the central damper, thereby influencing the behavior of the entire suspension.

The transmissibility \hat{T}_a is estimated as,

$$\hat{T}_a = \frac{\hat{\Gamma}}{\hat{\gamma}} \tag{6}$$

where $\hat{\Gamma} = -\omega^2 \hat{U}$ is the acceleration response of the system and $\hat{\gamma}$ is the input acceleration of the system. The transmissibility function is widely used in vibration analysis to assess the dynamic response of mechanical systems, specifically in terms of resonance frequency and stiffness variations. In this study, the use of the transmissibility function is intended primarily for a qualitative analysis of system behavior under different temperature conditions. It allows to observe how the resonance peak shifts with temperature, which reflects the changes in the effective stiffness of the suspension system. This approach is well-justified because the system is excited harmonically, and the transmissibility function provides a practical and commonly used indicator. As stated, the transmissibility \hat{T}_a is defined as the ratio of the amplitude of the response acceleration to the amplitude of the base excitation, with both quantities measured via accelerometers. It is assumed the measurement

device is placed on a rigid structure, ensuring uniform acceleration, which justifies the use of the transmissibility function. The system's response is characterized by how the resonance frequency evolves with temperature, reflecting the underlying changes in the stiffness of the suspension due to the temperature-induced material property variations. Results are given in Figure 5, depending on a dimensionless frequency f/f_0 where f is the frequency and f_0 is the resonant frequency (eigenfrequency) for the suspension without polymer, chosen as a reference frequency. Traditionally, the critical parameter of a suspension is the cutoff frequency, defined as the frequency above which the suspension begins to effectively attenuate the transmission of vibrations. This cutoff frequency may be related to the resonance frequency of the suspension. Since the analyses are formulated using a frequency ratio that consistently reflects both resonance and cutoff behavior, the conclusions obtained for the resonance frequency can thus be extended without loss of generality to the cutoff frequency. The transmissibility of the system (represented by colored lines in figure 5) across all temperatures is compared to the transmissibility of the system without polymer (depicted by the black line). Two main zones are defined to match the real conditions of use, they are graphically shown in figure 5.

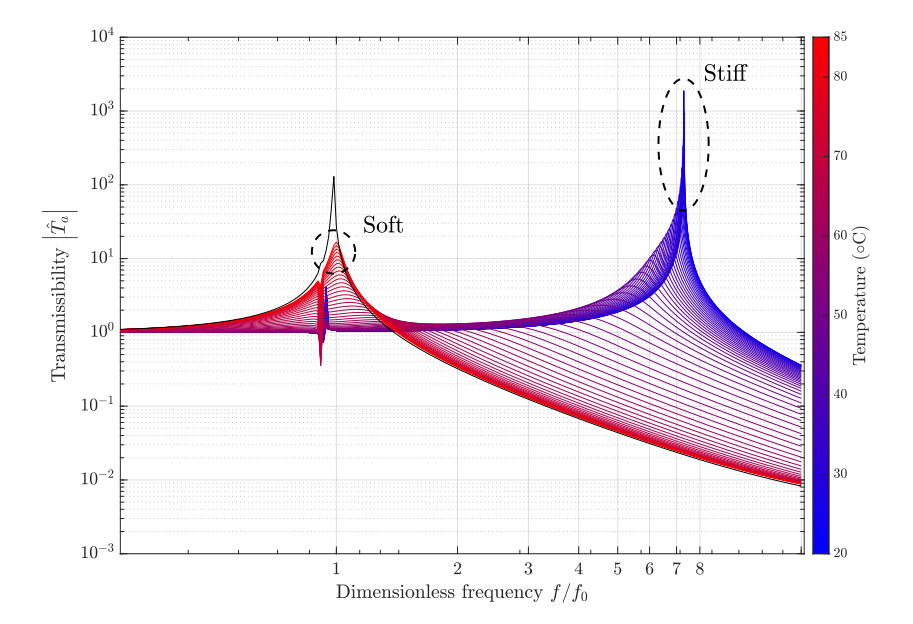


Figure 5: Transmissibility study on 65 temperature levels, colored lines from colorbar correspond to the transmissibility of the system under temperature conditions, black line correspond to the system without polymer (the three dampers are empty, which corresponds to the system's lowest stiffness configuration).

'Soft' represents a region where the system behaves akin to the full metal suspension, without the polymer, characterized by the cutoff frequency (or eigenfrequency) the suspension was initially designed with. This implies that the system is expected to maintain its initial stiffness to effectively filter low-amplitude and random excitations from the input. This zone is attained when T > 70 °C, the polymer has transitioned from the glassy state to the rubbery state. At this point, its storage modulus becomes significantly low, $E' < 10 \,\mathrm{MPa}$, exerting minimal impact on the damper and the overall system. Therefore, the system adopts a configuration in which frequencies above the cutoff frequency are filtered, ready to operate in the flexible configuration. 'Stiff' delineates a region where the central damper exhibits sufficient stiffness to alter the system's cutoff frequency (or eigenfrequency). This suggests that the central damper's rigidity overtakes the other two, resulting in a stiffer connection between the mobile mass and the base. This zone is achieved when T < 30 °C, indicating that the polymer is in its glassy state across the frequency range. At this point, its storage modulus is notably high, E' > 1 GPa, enabling the polymer to augment the stiffness of the central suspension. Consequently, the connection between the base and the mobile mass becomes rigid due to the central damper assuming a configuration where the cutoff frequency (or eigenfrequency) significantly deviates from its original design, yet the suspension is stiffer. This configuration is conducive to a rigid setup where the integrity of both the suspension and the mobile mass are at risk. It is possible to evaluate the variation of the stiffness between the soft and the rigid configuration which is more than 50 times. Finally, figure 6 illustrates the significant impact of polymer properties

on the eigenfrequency (or cutoff frequency) of the suspension, which can be controlled by adjusting the temperature.

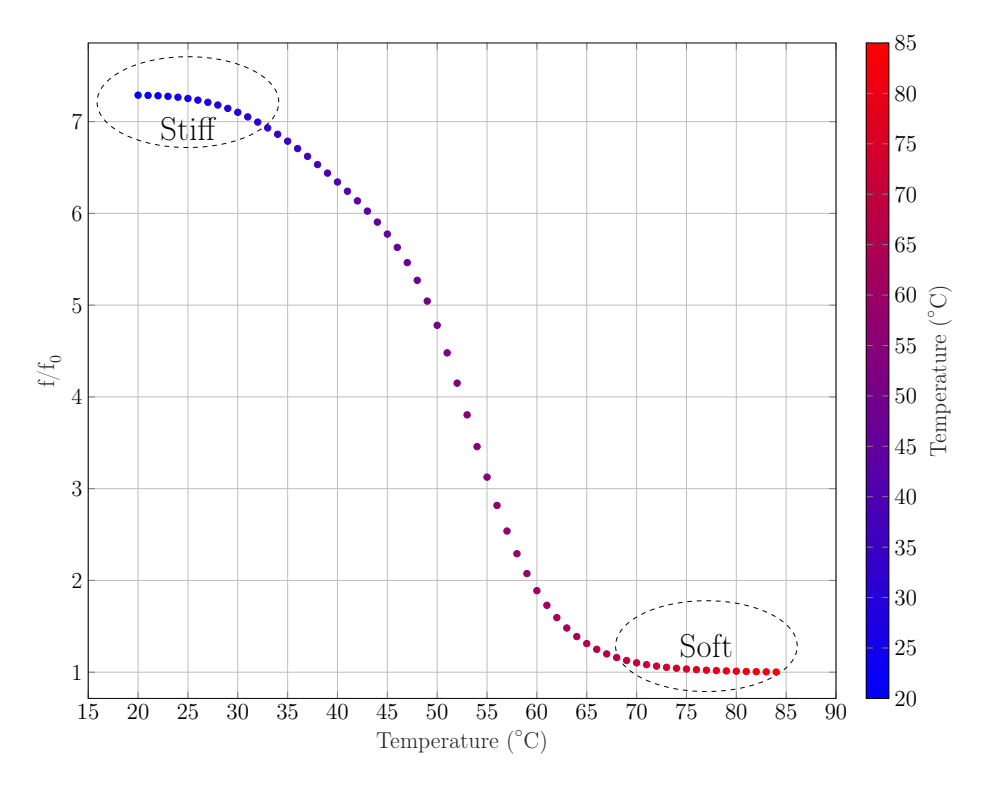


Figure 6: Evolution of the eigenfrequency of the suspension through the temperature range. It corresponds to the peak values of each transmissibility curve plotted in figure 5.

Although the primary focus of the present study is the tunability of the stiffness through thermal activation of the polymer, it must be emphasized that damping characteristics are also temperaturedependent. As the storage modulus decreases across the glass transition, the loss modulus and the associated damping ratio exhibit a non-monotonic behavior, with peak damping observed near the transition temperature (40–60 °C). This is consistent with the viscoelastic nature of the polymer and the 2S2P1D model. The broadening and lowering of the resonance peak in the transmissibility curves at intermediate temperatures (as seen in figure 5) indicate enhanced damping in that region. A quantitative estimation of damping values is provided in appendix D.

Experimental validation

The experimental campaign was conducted to validate the adaptive suspension concept. Furthermore, it also demonstrates that the design based on numerical simulations is effective.

4.1 Description of the experimental test-rig

The experimental setup for the vibration tests is depicted in figure 7. The structure is mounted on a vibrating table, which is equipped with a shaker, specifically the TIRA 27 kN. This shaker is employed to excite the structure clamped to the three inner rings. The excitation is configured as a random excitation in the Y-direction within the frequency range $[f_a; f_b]$. A three-axis accelerometer is positioned on the table to measure the input acceleration. Additionally, two three-axis accelerometers are put on the mobile mass to capture the response of the structure. The use of three-axis accelerometers allows to check that the response is purely translational and not rotational. A system that minimally influences the mechanical properties without affecting the stiffness is chosen to heat the polymer. Ultimately, a heat gun with multiple settings is chosen, allowing to adjust the temperature applied to the polymer. This one is continually monitored using a thermal camera to provide real-time feedback on the applied temperature. Figure 8 illustrates the thermal field measured on the polymer: lower values are observed next to the metallic parts but the global field is almost homogeneous. Linearity of experimental results is verified by testing other amplitudes of excitation.

The camera provides three temperature measurements: a mean value, a maximum value, and a minimum value. This camera is also able to measure the ambient temperature of the room with an other sensor. Moreover, a thermocouple is immersed in the polymer to provide an additional method

80,0

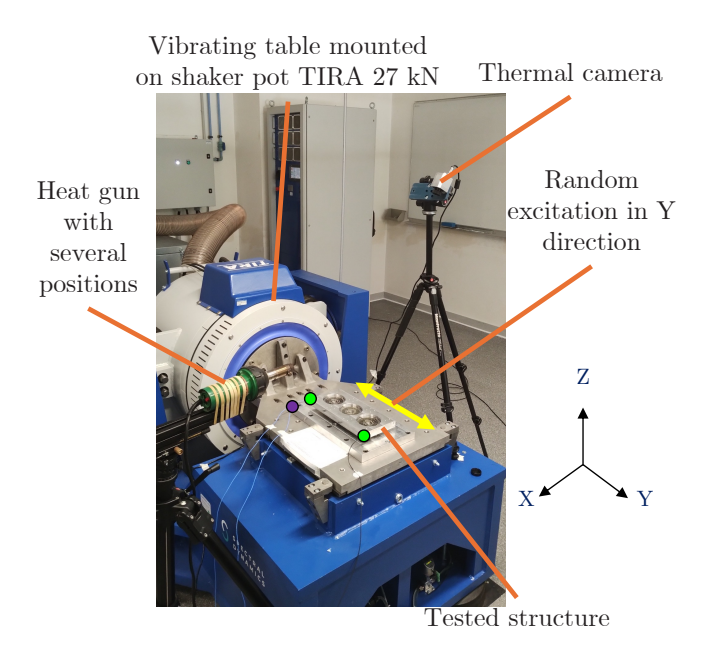


Figure 7: View of the set-up. Green points are the positions of the 3D accelerometers for the payload. Purple point is the position of the 3D accelerometer for the base.

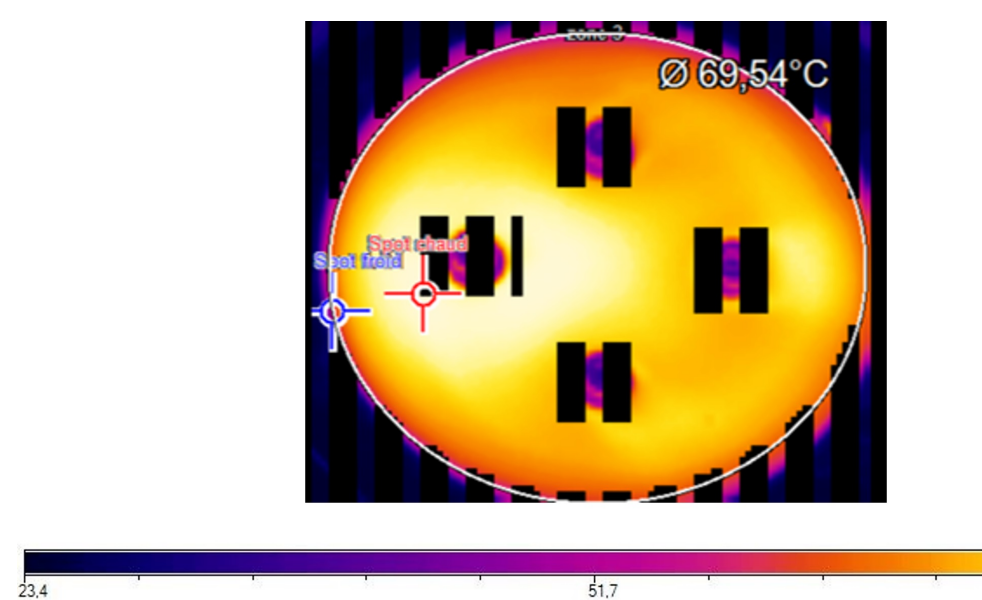


Figure 8: The thermal camera imagery of the polymer under observation reveals key temperature distributions in real time. Non-measured areas are denoted by black lines, while the highest temperature point within the measured field is marked in red, and the lowest temperature point is marked in blue. A white circle delineates the region where the mean temperature is calculated, excluding the unmeasured regions. The corresponding mean temperature value is displayed within the white circle. The legend provides temperature readings for each point captured by the camera, with $^{\circ}$ C as unit.

of measurement. As shown in figure 3, the polymer integrated into the central damped is fastened at its center to the inner ring using screws. The polymer sample is machined to seamlessly fit with the outer ring; however, a thin aluminum ring (referred to as a clamping ring) is added to improve the connection between the outer ring and the sample.

Level	0	1	2	3	4	5	6	7	8	9
Mean	20.990	24.754	32.637	37.048	41.802	45.882	53.805	56.975	58.665	60.487
StD	1.498	1.503	0.741	1.014	1.776	2.399	1.454	2.150	2.105	1.381

Table 4: Estimation of the average temperature (Mean) and standard deviation (StD) of temperature for each of the ten experimental levels

4.2 Results and Discussions

The results of this section are obtained for six temperature cycles with the same set of samples. Each cycle encompassed ten temperature levels: these levels (Level 1 to 9) correspond to the 9 settings of the heat gun and the last additional level (Level 0) corresponds to a one measurement at the ambient temperature of the room. Table 4 gives the mean temperature as well as the temperature standard deviation for the ten levels. At each level, 10 averages of the random excitation at the base within the frequency range $[f_a; f_b]$ are done to average the results. This configuration aims to mitigate measurement noise; however, residual variability may still persist due to imperfect contacts in the experimental setup. It is interesting to mention that the maximum strain estimated in both simulations (0.12%) and experiments (0.16%) remains below 1%. Considering the work done by Butaud et al. [2018] demonstrating that nonlinearities only become significant beyond 2% strain, the tBA-PEGDMA can be considered as behaving linearly under small deformations.

The measured acceleration transmissibilities for all the temperature settings of the heat gun are presented in figure 9. Results coming from numerical simulations for the soft and for the rigid case are added to the figure as indicators of the limit configurations. The experimental result obtained for the reference case without polymer coherently corresponds in terms of resonance frequency to the numerical soft case as the material has no impact in this configuration. Then, as expected, the effects of temperature are readily discernible and lead to changes in both the stiffness and the damping of the structure, such that the resonance frequency is modified. The variation domain is large with a stiff case with a resonance frequency corresponding to 5.5 times the soft one, against more than 7 for the numerical results. A damping estimation of the system is shown in D.

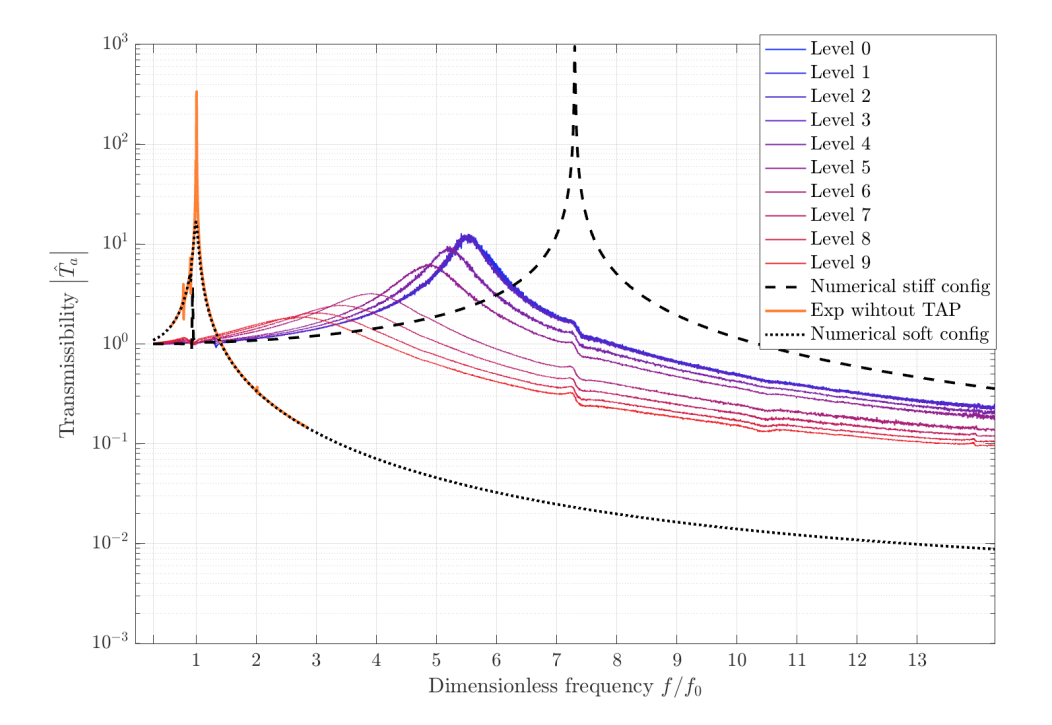


Figure 9: Evolution of the experimental acceleration transmissibility for ten heat levels (colored curves) - the numerical transmissibilities in the soft (...) and stiff (---) configurations are indicated for comparison, as well as the experimental transmissibility without polymer (--)

Figure 10 presents a numerical-experimental comparison of the evolution of the resonance frequency ratio with the temperature. For each cycle test, the ratio is built from the resonance frequency f_c determined during the cycle, and the reference resonance frequency f_0 .

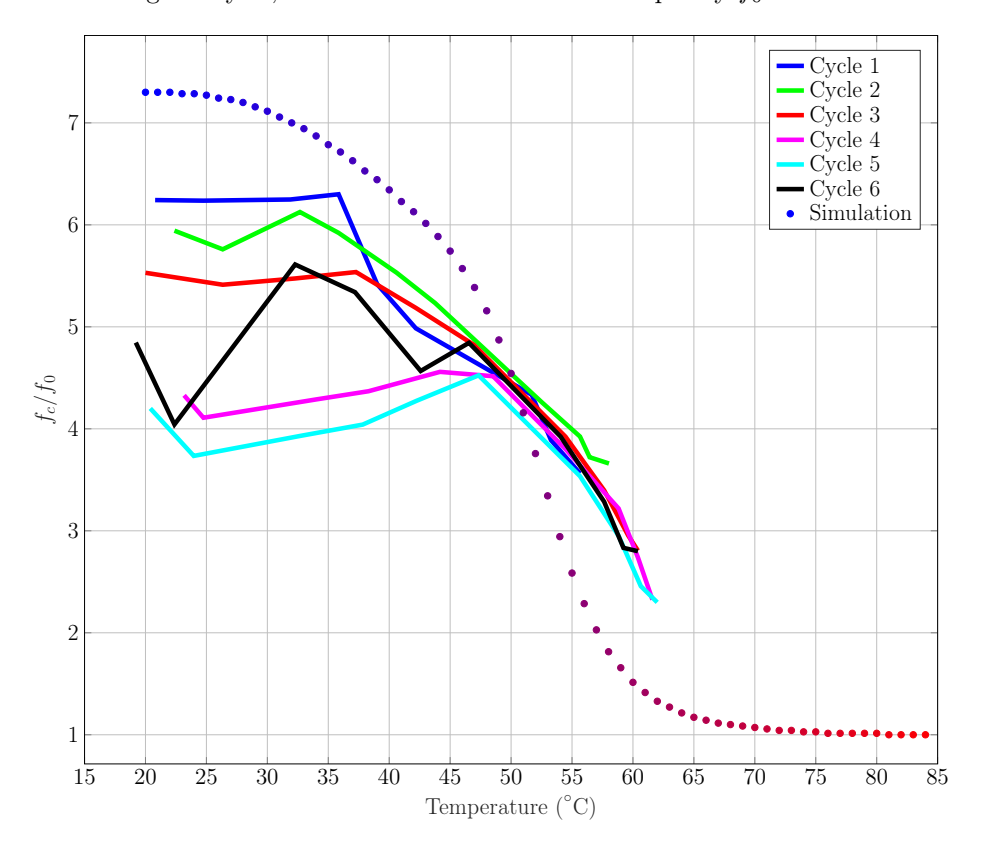


Figure 10: Evolution of the resonance frequency ratio f_c/f_0 depending on the temperature during each cycle: f_c is the resonance frequency for each cycle and f_0 is the chosen reference frequency at 85 °C (colored lines). The evolution predicted by the numerical simulation is given for comparison pupose (colored dots).

The criteria to estimate the resonance frequency is here the peak criteria, but similar results are obtained using the phase criteria (Appendix B). Numerical simulations are thermomechanical simulations considering the variation of the temperature field within the viscoelastic material as presented in Appendix C. Some differences are notable compared to the numerical model, although the overall trend is promising. Firstly, the expected temperature levels to reach the soft operating region are not attained ($T_{max} \approx 60$ °C). As shown by the thermal simulation in Appendic C, the non-uniform temperature distribution within the polymer presents an issue. To address this, a heating system using conductive wires following a pattern within the polymer could be considered. However, this solution is deemed potentially too costly for a proof-of-concept study such as described in this investigation. Secondly, variations in behavior at low temperatures $(T < 40 \,^{\circ}\text{C})$ are observed in the different results. This is partly due to certain assumptions made in the simulation that are questionable during experimental validation, such as perfect assembly between the polymer and the suspension, and firm attachment to the outer ring. This is further confirmed by the degradation of assembly quality over the cycles, resulting in decreased rigidity of the connections and consequently lowering the resonance frequency to unexpected levels. A possible improvement would be to directly vulcanize the polymer in place within the suspension structure. This would ensure optimal contact conditions across all temperatures and eliminate the observed variations due to mechanical gaps. Such a solution is under consideration for future iterations of the system. To further investigate the observed discrepancies between the numerical and experimental results, two additional numerical studies have been conducted. These simulations aim to assess the influence of imperfect mechanical contact between the polymer and the suspension, and non-uniform temperature distribution within the polymer, which may both significantly impact the overall system response. The details and results of these simulations are provided in and C and E respectively.

To further elucidate the dynamic behavior of the system, phase response between input and output accelerations is analyzed, revealing additional discrepancies between simulations and experiments, particularly in the transitional thermal regime. These effects are attributed to thermal lag

and imperfect mechanical contacts and are discussed in B. Also, some quantitative values are given in B to aid in understanding the study. These analyses help to justify the observed deviation in the low-temperature range and reinforce the robustness of the proposed concept taking into account realistic experimental uncertainties. Nevertheless, the behavior of the system aligns with what was calculated during the simulations, particularly regarding the effect of changing the resonance frequency. From an application perspective, the system is not intended to operate with fine control over intermediate temperature states. Rather, the goal is to reach distinct mechanical states — one soft and one stiff — by applying either a high temperature (above 70 °C) or a low temperature (below 30 °C). The system is not designed for continuous modulation of stiffness during dynamic operation, but rather to switch between two stable configurations: rigid and soft. Intermediate temperatures can produce non-monotonic trends due to concurrent changes in contact quality and material modulus. In this context, the intermediate discrepancies have a limited impact on the intended functionality.

Based on these conclusions, a specific recalibration process of the polymer parameters has been performed considering two key refinements: (i) a reduction of the bonded surface area to account for imperfect mechanical contact, (ii) a spatially non-uniform temperature distribution at the polymer surface, modeled using a 50% heat transfer coefficient between the heater and the polymer. For each temperature cycle, an optimal bonded surface reduction was identified to minimize the frequency discrepancy. The estimated contact areas progressively decrease with each cycle: 31% of the diameter surface for cycle 1, 27% for cycle 2, 21% for cycle 3, 11% for cycle 4, 9% for cycle 5, and 14% for cycle 6. This trend suggests a degradation or instability of the contact interface over repeated thermal loading. Figure 11 presents the experimental and numerical suspension transmissibilities for each temperature level.

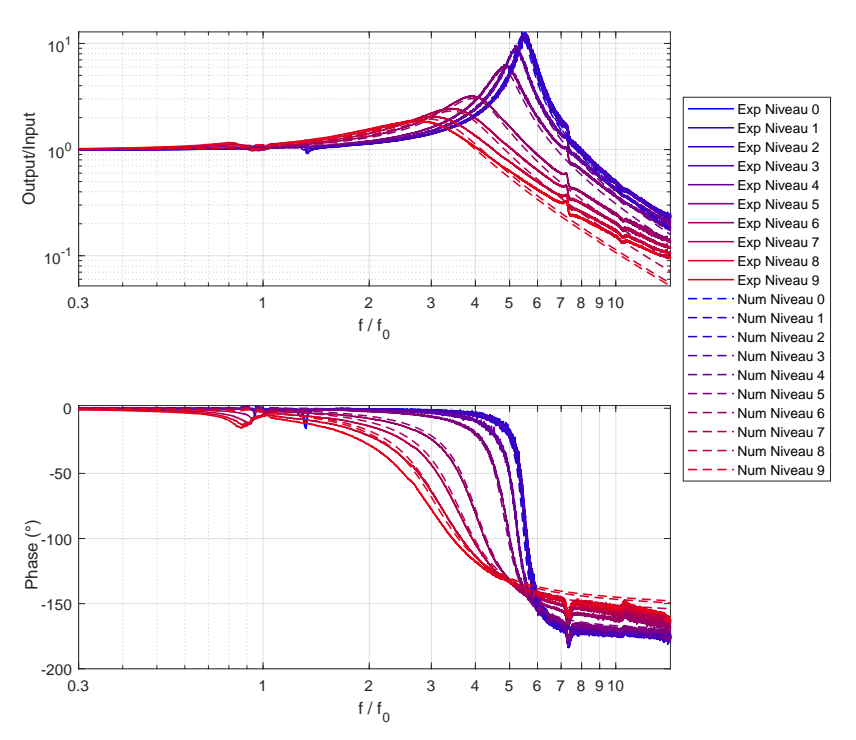


Figure 11: Comparison of experimental (Cycle 3) transmissibility and phase responses (solid lines) with numerical predictions (dashed lines), after calibration of the polymer's stiffness and damping parameters in the numerical model based on experimental data.

The results reveal an excellent agreement over the considered frequency range, with the resonance peaks and associated damping behavior closely matching. In particular, the phase shift between input and output signals exhibits negligible deviation across the full bandwidth, indicating that the model accurately captures not only the amplitude but also the time dynamics of the system.

4.3 Quantification of the performance

To quantify the experimental performance of the suspension, a factor α quantifying the stiffness change and defined as,

$$\alpha_i = \left(\frac{f_{c,i}}{f_0}\right)^2 \tag{7}$$

is calculated and given in Table 5. $f_{c,i}$ corresponds to the resonance frequency obtained for cycle i (i=[1:6]) and f_0 is the reference resonance frequency obtained without polymer. Experimental

α_i (Cycle i)	α_1	α_2	α_3	α_4	α_5	α_6
Value	39.7	37.5	30.7	20.4	20.7	31.4

Table 5: Evolution of α through cycles.

thermal transitions are observed over a range of 3–5 minutes (heating) and around 10 minutes (passive cooling), depending on ambient conditions. While relatively slow, these timescales are acceptable for applications allowing implementation time, such as landing or takeoff phases where stability is prioritized over speed. It can be concluded that the increase in stiffness that can be achieved with the polymer between a static configuration and a dynamic one is significant, with a coefficient greater than 20 obtained experimentally.

5 Conclusion

In this work, a suspension system with high static and low dynamic stiffness control ability is proposed and demonstrated in a bench test setup where the suspension is connected to a base and a payload. The suspension is composed of three dampers, the central one is charged with a temperature-sensitive polymer, the tBA/PEGDMA. This polymer is used to tune the stiffness of the suspension via temperature control. When the applied temperature is below the glass transition temperature of the polymer, the suspension stiffens, resulting in a significant increase in the cutoff frequency (or eigenfrequency), thereby altering the vibration transmission behavior. Instead of filtering a broad bandwidth, this stiffness adjustment enables the suspension to become very rigid, preventing undesired relative displacement between the base and the payload in specific scenarios. Conversely, when the applied temperature exceeds the transition temperature, the contribution of the polymer is negligible, and the suspension behavior reverts to its initial state. The proof-of-concept prototype used in this study exhibited intriguing behavior predicted by numerical simulation, thus validating the proof of concept and paying the way for technological enhancements to better align with numerical predictions and achieve the two desired operating zones initially targeted in this study. Future work will include the integration of localized heating systems, such as embedded resistive wires or conductive polymers, to reduce response time and ensure uniform activation. Additionally, direct polymer casting into the suspension structure is considered to eliminate mechanical gaps and improve repeatability.

Acknowledgments

This work has been achieved in the frame of the EIPHI Graduate school (contract ANR-17-EURE-0002), Bourgogne Franche-Comté Region and the ANRT (CIFRE), France. Authors are grateful to the french company THALES LAS France for their financial support.

A Chemical definition of tBA-PEGDMA

tBA/PEGDMA is elaborated at the FEMTO-ST Department of Applied Mechanics and synthesized by manually mixing 95 % tert-Butyl Acrylate (tBA) monomer with 5 % poly(ethylene glycol) dimethacrylate (PEGDMA) cross-linking agent. Additionally, a photo-initiator, 2,2-dimethoxy-2-phenylacetophenone (DMPA), is incorporated into the mixture at approximately 0.5 %, a graphical representation is shown in Figure 12. The solution is then injected between two carefully cleaned glass plates, with an elastic joint used both to seal the plates and to control the thickness of the resulting polymer film. Polymerization is initiated by exposing the mixture to UV light for 10 minutes, followed by a post-curing step involving heating at 90 $^{\circ}$ C for 60 minutes.

Based on prior research, it is assumed that the resulting polymer is a thermoset amorphous material, and all raw polymer samples are cut sufficiently far from the edges to ensure homogeneity. Samples intended for subsequent analyses are machined to generate adequate shapes for experimental characterization.

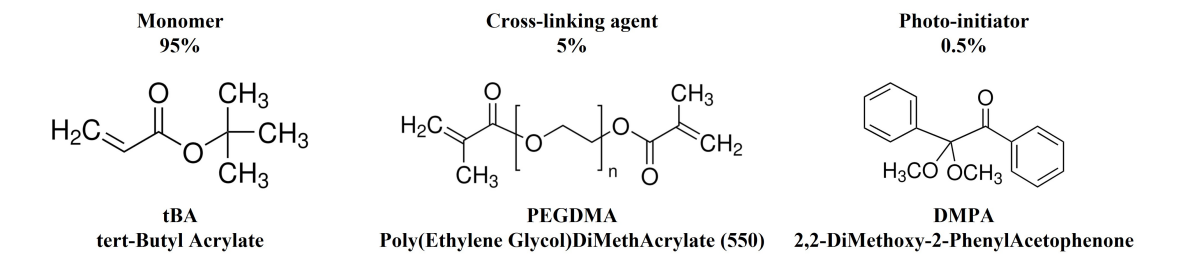


Figure 12: Graphical representation of the polymer

B Phase criteria analysis

Another way to estimate the resonance frequency than using the peak frequency is to consider the frequency at which the phase shift between excitation and response reaches $\pi/2$. This phase-based criterion is known to better account for damping effects and is commonly used in the context of vibration isolation. Although a complex modal analysis would be required to fully characterize the viscoelastic system, it has been intentionally maintained a simplified frequency-based comparison to preserve consistency with the transmissibility analysis and to facilitate experimental implementation. Figure 13 presents the evolution of the frequency ratio to the reference frequency f_0 using the peak amplitude criteria (solid line) and using the phase- $\pi/2$ criteria (dashed line) over the temperature range. The coherence between the two curves provides additional confidence in the validity of the experimental measurements and their correspondence with the simulated results.

C Thermal analysis of the damper with polymer

In order for the suspension behavior to switch from "stiff" to "soft" precisely and quickly, it is necessary to ensure that the temperature is uniform and clearly above or below the glass transition temperature. To ensure this, it is necessary to control the temperature using a temperature sensor and a control loop that acts on the heat source. To better understand the thermal behavior of the viscoelastic part, particularly the temperature distribution resulting from an external temperature stimulus on its surface, a thermal simulation of the polymer-filled damper is conducted. This simulation is crucial because it allows to understand the impact of the surface temperature measured by the thermal camera, and to estimate the effective temperature inside the polymer, which greatly influences its mechanical behavior. Two aspects are studied: firstly, the emergence of a temperature gradient across the thickness, and secondly, the presence of a temperature gradient along the surface. To study the temperature gradient across the thickness, a thermal simulation is performed considering that a constant temperature T_0 between 20 °C and 85 °C is applied to the surface of the polymer. This temperature corresponds to the average temperature measured by the thermal camera. All other surfaces are subjected to convection conditions, either with the steel of the suspension in the contact areas or with the air in the non-contact areas. An ambient temperature corresponding to the temperature measured by the thermal camera sensor is applied to surfaces not affected by the application of temperature T_0 and without contact with another material. The thermal behavior of the viscoelastic part is shown for an application of temperature T_0 in figure 14. This simulation confirms the emergence of a gradient that affects the temperature distribution in the polymer, thereby

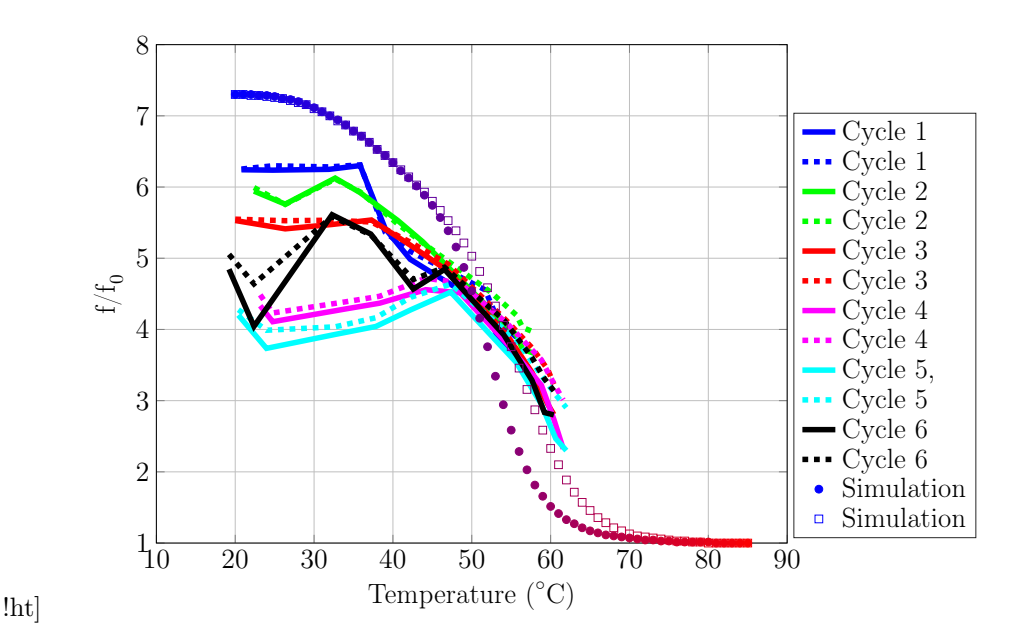


Figure 13: Evolution of the experimental eigenfrequency (solid line) and experimental phase- $\pi/2$ frequency (dashed line) for the six cycles over the entire range of temperatures. The numerical results are added for comparison purposes, using the peak criteria (simulation - markers in dots) and the $\pi/2$ phase criteria (simulation - markers in squares).

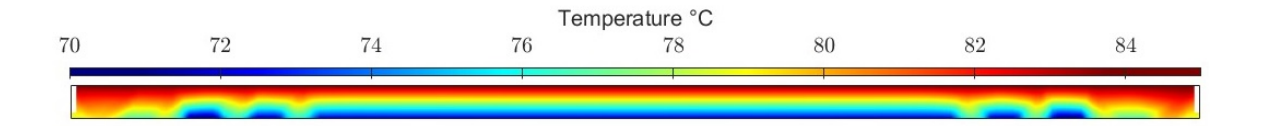


Figure 14: Temperature field in a cross section of the polymer for an applied surface temperature $T_0 = T_{mes} = 85$ °C. The lowest temperature in the material is $T_{real} = 73$ °C

modifying its mechanical behavior. In order to take this into account in the study, all simulations performed are thermomechanical coupled simulations in order to accurately describe the thermal field distribution.

Besides, thermal gradients occur on the polymer surface due to localized heating and the presence of metallic components acting as thermal sinks. To study this phenomenon, a two-step coupled thermo-mechanical analysis was performed. First, a steady-state thermal simulation was carried out by applying a controlled surface temperature to the upper face of the polymer, mimicking the experimental heating conditions. The ambient temperature (20 °C) was imposed on the rest of the system, including the mobile mass, metal parts, and support ring. The boundary condition of the thermal simulation are illustrated in figure 15. In a first configuration, the entire upper surface of the polymer was subjected to a uniform temperature of 85 °C. In subsequent simulations, the heated surface was progressively reduced to 90%, 70%, 50%, and 30% of the upper surface area. On the remaining portion of the top surface (i.e., the unheated area), the applied temperature is defined based on an empirical model developed using thermal camera measurements conducted during experimental tests. Figure 16 presents the maximum and minimum surface temperatures recorded during 4 of the 6 cycles (3,4,5,6). To estimate the minimum temperature on the unheated portion of the surface, an empirical power-law model was fitted to these measurements. The resulting model

$$T_{\min}(T_{\max}) = 1.07 \cdot T_{\max} + 5.61.$$

This expression represents the surface heat diffusion behavior due to the increasing role of lateral conduction losses at lower heating ratios. The coefficient of determination is $R^2 = 0.998$) confirming that this expression provides a good approximation of the measured data.

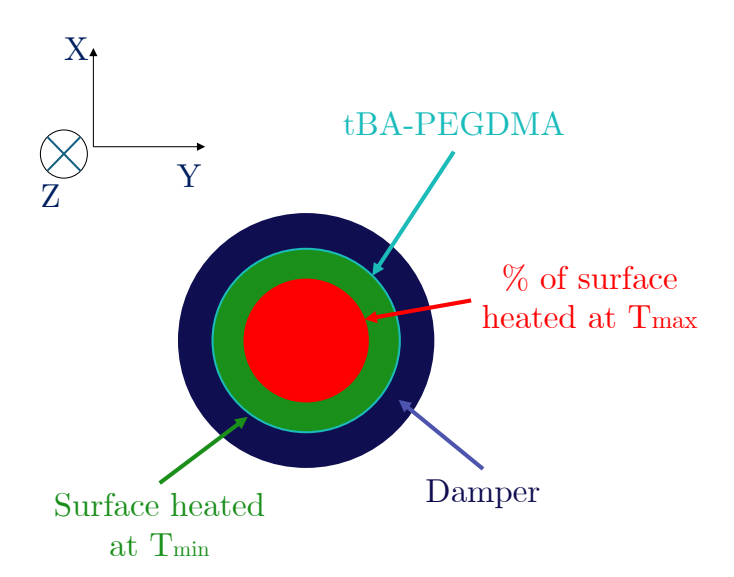


Figure 15: Boundary conditions to simulate non-uniform heating of the polymer, with a variable heated surface.

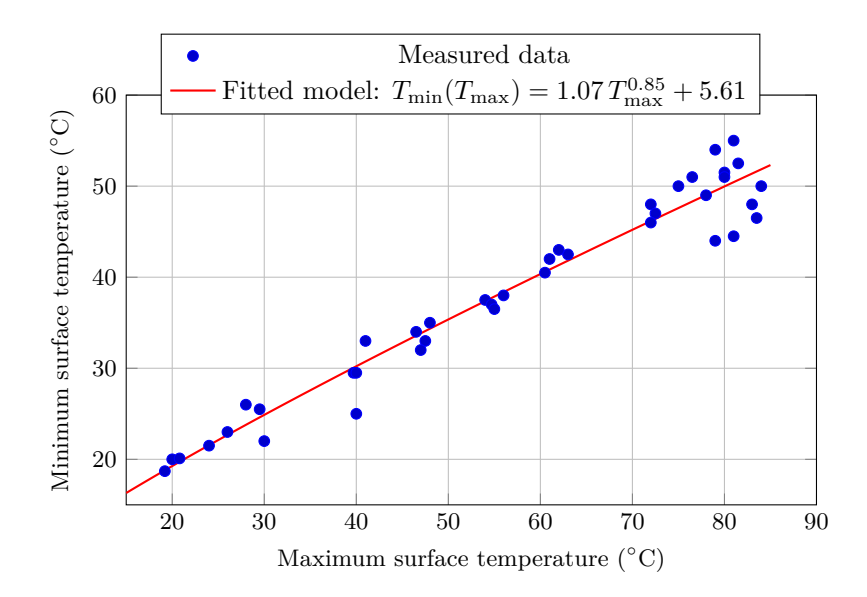


Figure 16: Power-law fit of minimum surface temperature as a function of maximum surface temperature measured by the thermal camera.

This empirical law was then used to define the surface temperature to apply in the non-heated portion of the polymer in the numerical simulation, providing a realistic approximation of the experimentally observed thermal field. This model captures the observed thermal behavior under partial heating conditions and improves the realism of the simulated thermal gradient. Figure 17 shows the results of the overvoltage frequency evolution of the simulated thermal gradient with the experimental data considering only the maximum of temperature measured, for each level of the heat gun, with the thermal camera. The results show that the discrepancy observed in the medium-hightemperature range is significantly reduced when accounting for non-uniform heating. In particular, the progressive softening of the polymer is delayed under partial heating, which better matches the behavior observed during experimental testing.

The results show that the estimated percentage of the diameter heated to the maximum temperature is between 50 and 70% for all cycles. This confirms that thermal heterogeneities within the polymer — due in particular to incomplete surface heating — can explain the delay in softening behavior and the discrepancy observed between simulations and experimental measurements. This effect must be taken into account in future designs, particularly in systems where heating cannot be applied uniformly or where thermal control is limited.

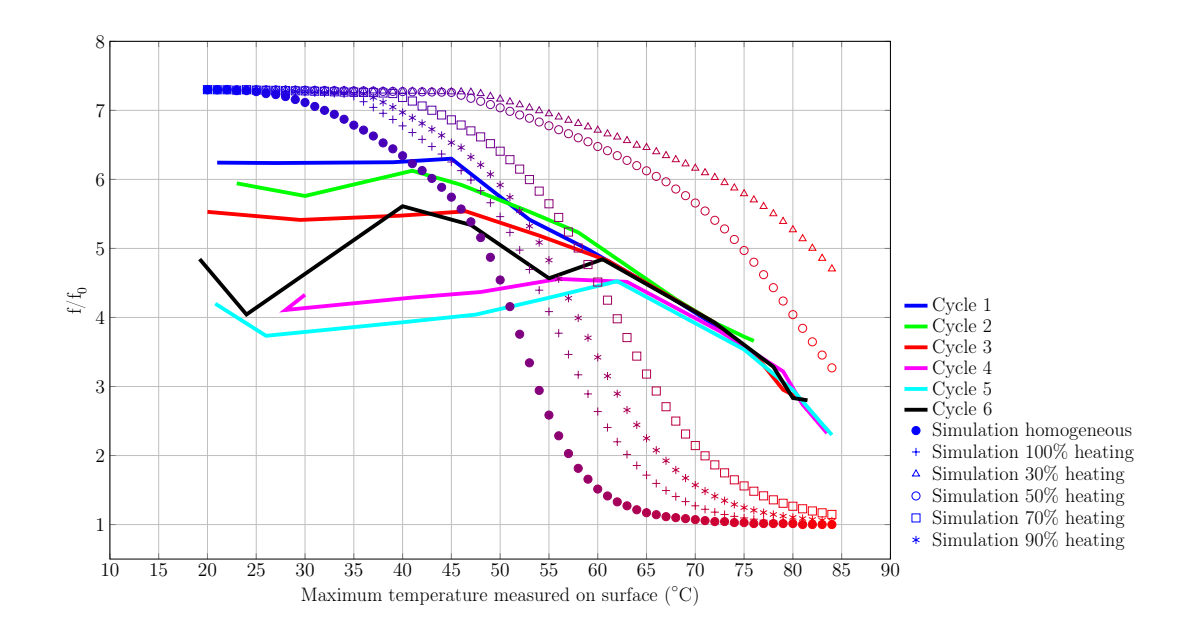


Figure 17: Evolution of the eigenfrequency as a function of temperature for different heating conditions: comparison between simulations and experimental data. The temperature axis corresponds to the maximum temperature applied on the surface.

D Numerical analysis of damping of the system with a temperature-driven polymer and comparison with experimentations

With regard to the numerical study (figure 6), in order to provide quantitative information on the influence of temperature on damping, the effective damping ratio ξ_{eff} was estimated directly from the complex eigenvalues of the system at each temperature. In the glassy state (20 °C), ξ_{eff} is approximately 0.01%; near the transition temperature (40–58 °C), it increases to around 43%; and in the rubbery state (>80 °C), it drops again to 3%. This variation confirms the expected viscoelastic behavior Butaud et al. [2018], with a damping peak associated with the glass transition of the tBA-PEGDMA polymer. These results are shown in figure 18.

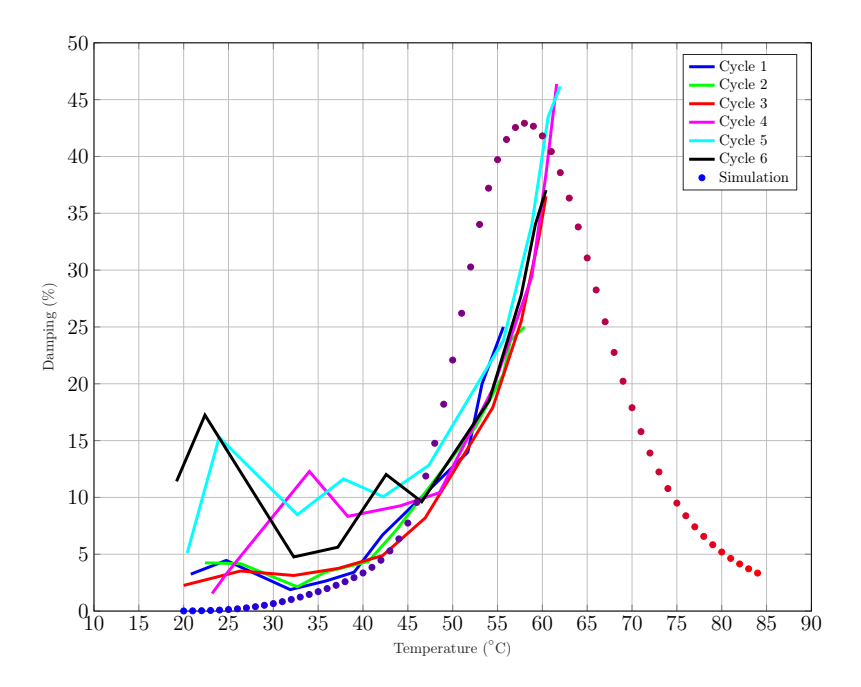


Figure 18: Evolution (numerical and experimental) of the damping of the system depending on the temperature

60

Considering the experimental study (figure 6, in order to compare it with the numerical results, the global behavior of the system is similar, although the damping values are affected by imperfections described in Appendix C, as imperfect contacts introduce additional frictional damping. The experimental damping ratio ξ_{exp} ranges from 2% to 11% in the glassy state, and increases up to 46% near the transition region. However, since the highest temperature reached experimentally was only 62 °C, the decrease in damping observed in the numerical study at higher temperatures could not be verified experimentally. These results are also presented in figure 18.

${f E}$ Numerical study of imperfect contact

In order to explain the discrepancies observed at low temperatures between the simulations and the experiments (figure 10), additional simulations were performed to account for the imperfect mechanical contact between the polymer and the outer ring of the suspension. In the experimental setup, the polymer sample is inserted inside the ring, but perfect adhesion is not guaranteed, especially at low temperatures when thermal expansion is minimal.

To model this effect, different contact conditions were simulated by varying the effective bonding surface between the polymer and the ring. This was achieved by defining two boundary segments at the interface: one where a continuity condition is enforced (representing the bonded regions), and the other where a free condition is applied (representing the unbounded regions). Six configurations were considered, corresponding to 5%, 10%, 30%, 50%, 70%, and 90% of the circumference of the interface in contact.

The same analysis as described in Section 3.3 was performed for each case, allowing comparison of the resonance behavior under different interface conditions. Figure 19 illustrates the boundary conditions applied in the model. Figure 20 compares the evolution of the eigenfrequency with the

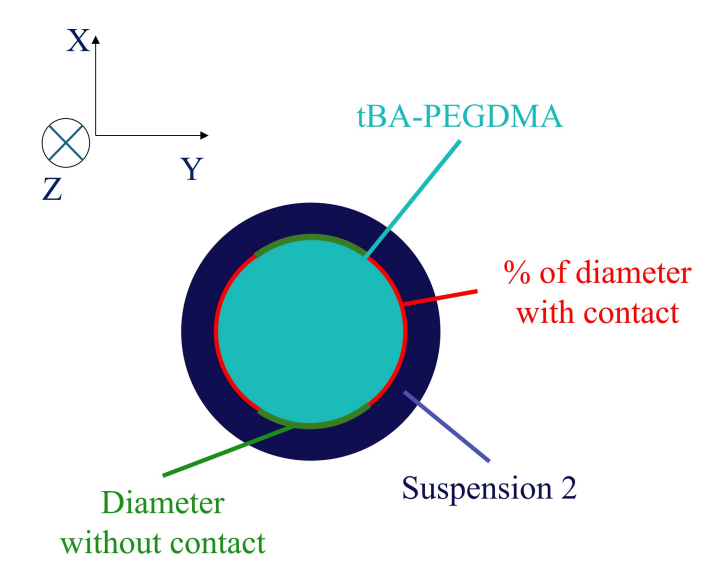


Figure 19: Boundary condition configuration to simulate imperfect contact at the polymer-ring interface. The red part is the interface circumference in contact, the green part is the interface circumference free. The cyan represents the polymer in the suspension in blue.

temperature obtained through simulation for different contact conditions to the evolution obtained during the different cycle tests. These results show that an imperfect contact — particularly below 70% — leads to a significant shift in eigenfrequency (or cutoff frequency), consistent with the discrepancies observed experimentally at low temperatures. The estimated percentage of the polymer diameter in contact with the outer ring of the suspension is between 30 and 50% for cycles 1 and 2, around 30% for cycle 3, between 10 and 30% for cycles 4 and 6, and between 5 and 30% for cycle 5. These results highlight that imperfect contact is a significant source of discrepancy, particularly at low temperatures, and must be taken into account in future design improvements.

References

P. Alabuzhev. Vibration protection and measuring systems with quasi-zero stiffness. CRC Press, 1989.

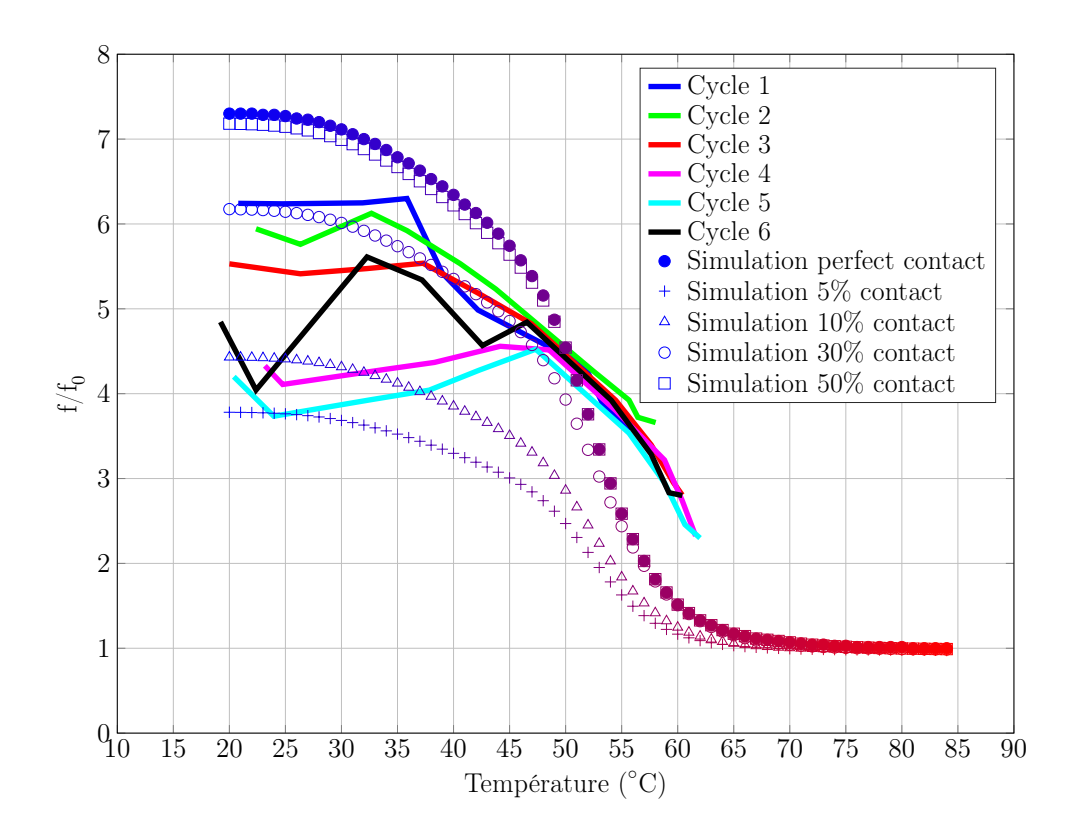


Figure 20: Evolution of the frequency ratio with temperature for various contact conditions compared to experimental trends.

- P. Butaud, E. Foltête, and M. Ouisse. Sandwich structures with tunable damping properties: On the use of shape memory polymer as viscoelastic core. *Composite Structures*, 153:401–408, 2016.
- P. Butaud, M. Ouisse, V. Placet, F. Renaud, T. Travaillot, A. Maynadier, G. Chevallier, F. Amiot, P. Delobelle, E. Foltête, and C. Rogueda-Berriet. Identification of the viscoelastic properties of the tBA/PEGDMA polymer from multi-loading modes conducted over a wide frequency—temperature scale range. *Polymer Testing*, 69:250–258, 2018. ISSN 01429418. doi: 10.1016/j.polymertesting. 2018.05.030.
- C. Cai, J. Zhou, K. Wang, H. Pan, D. Tan, D. Xu, and G. Wen. Flexural wave attenuation by metamaterial beam with compliant quasi-zero-stiffness resonators. *Mechanical Systems and Signal Processing*, 174:109119, 2022a.
- C. Cai, J. Zhou, K. Wang, D. Xu, and G. Wen. Metamaterial plate with compliant quasi-zero-stiffness resonators for ultra-low-frequency band gap. *Journal of Sound and Vibration*, 540:117297, 2022b.
- V. Candido de Sousa, C. Sugino, C. De Marqui Junior, and A. Erturk. Adaptive locally resonant metamaterials leveraging shape memory alloys. *Journal of Applied Physics*, 124(6), 2018.
- A. Carrella, M. Brennan, and T. Waters. Static analysis of a passive vibration isolator with quasi-zero-stiffness characteristic. *Journal of sound and vibration*, 301(3-5):678–689, 2007.
- Y. Chai, X. Jing, and X. Chao. X-shaped mechanism based enhanced tunable qzs property for passive vibration isolation. *International Journal of Mechanical Sciences*, 218:107077, 2022.
- K.-C. Chuang, X.-F. Lv, and Y.-H. Wang. A bandgap switchable elastic metamaterial using shape memory alloys. *Journal of Applied Physics*, 125(5), 2019.
- E. Collard and T. Fabrice. Element de suspension pour la liaison mecanique d'une charge suspendue dans un support. 2013.
- G. Dong, X. Zhang, S. Xie, B. Yan, and Y. Luo. Simulated and experimental studies on a high-static-low-dynamic stiffness isolator using magnetic negative stiffness spring. *Mechanical Systems and Signal Processing*, 86:188–203, 2017.

- H. Han, L. Tang, J. Wu, S. Sun, P. Yin, and D. Cao. Origami-inspired isolators with quasi-zero stiffness for coupled axial-torsional vibration. *Aerospace Science and Technology*, 140:108438, 2023.
- K. Jaboviste, E. Sadoulet-Reboul, N. Peyret, C. Arnould, E. Collard, and G. Chevallier. On the compromise between performance and robustness for viscoelastic damped structures. *Mechanical* Systems and Signal Processing, 119:65–80, 2019.
- M. N. Kalat, M. Staszczak, L. Urbański, C. Polvorinos-Fernández, C. A. Vega, M. Cristea, D. Ionita, A. D. Lantada, and E. A. Pieczyska. Investigating a shape memory epoxy resin and its application to engineering shape-morphing devices empowered through kinematic chains and compliant joints. *Materials & Design*, 233:112263, 2023.
- K. Kocak and C. Yilmaz. Design of a compliant lever-type passive vibration isolator with quasi-zero-stiffness mechanism. *Journal of Sound and Vibration*, 558:117758, 2023.
- M. Li, W. Cheng, and R. Xie. A quasi-zero-stiffness vibration isolator using a cam mechanism with user-defined profile. *International journal of mechanical sciences*, 189:105938, 2021.
- M. Li, Y. Li, X. Liu, and F. Dai. A quasi-zero-stiffness vibration isolator using bi-stable hybrid symmetric laminate. *Composite Structures*, 299:116047, 2022.
- C. Liu, W. Zhang, K. Yu, T. Liu, and Y. Zheng. Quasi-zero-stiffness vibration isolation: Designs, improvements and applications. *Engineering Structures*, 301:117282, 2024.
- X. Liu, X. Huang, and H. Hua. On the characteristics of a quasi-zero stiffness isolator using euler buckled beam as negative stiffness corrector. *Journal of Sound and Vibration*, 332(14):3359–3376, 2013.
- V. Srivastava, S. A. Chester, and L. Anand. Thermally actuated shape-memory polymers: Experiments, theory, and numerical simulations. *Journal of the Mechanics and Physics of Solids*, 58(8): 1100–1124, 2010. ISSN 0022-5096. doi: 10.1016/j.jmps.2010.04.004.
- J. Sun, L. Du, F. Scarpa, Y. Liu, and J. Leng. Morphing wingtip structure based on active inflatable honeycomb and shape memory polymer composite skin: a conceptual work. Aerospace Science and Technology, 111:106541, 2021.
- Q. Wang, J. Zhou, K. Wang, Q. Lin, D. Xu, and G. Wen. A compact quasi-zero-stiffness device for vibration suppression and energy harvesting. *International Journal of Mechanical Sciences*, 250: 108284, 2023.
- L. Xiao, X. Sun, L. Cheng, and X. Yu. A 3d-printed quasi-zero-stiffness isolator for low-frequency vibration isolation: Modelling and experiments. *Journal of Sound and Vibration*, 577:118308, 2024.
- J. Xu and J. Jing. Low-frequency band gaps in quasi-zero stiffness locally resonant metamaterial shaft. *International Journal of Mechanical Sciences*, 267:108992, 2024.
- K. Ye, J. Ji, and R. Fitch. Further investigation and experimental study of an origami structure-based quasi-zero-stiffness vibration isolator. *International Journal of Non-Linear Mechanics*, 157: 104554, 2023.
- Z. Zhao, X. Cui, Y. Yin, Y. Li, and M. Li. Thermal tuning of vibration band gaps in homogenous metamaterial plate. *International Journal of Mechanical Sciences*, 225:107374, 2022.
- S. Zuo, D. Wang, Y. Zhang, and Q. Luo. Design and testing of a parabolic cam-roller quasi-zero-stiffness vibration isolator. *International Journal of Mechanical Sciences*, 220:107146, 2022.